

SCIENTIFIC REPORTS



OPEN

Good Biocompatibility and Sintering Properties of Zirconia Nanoparticles Synthesized via Vapor-phase Hydrolysis

Received: 24 May 2016
Accepted: 22 September 2016
Published: 11 October 2016

Jigang Wang^{1,2,*}, Wenyan Yin^{3,*}, Xiao He³, Qiang Wang^{1,2}, Ming Guo¹ & Shaowei Chen⁴

ZrO₂ nanoparticles were synthesized by a vapor-phase hydrolysis process, and characterized in terms of crystalline structures, hardness and microstructures by X-ray diffraction, Vickers hardness test method, and atomic force microscopy (AFM) measurements. Moreover, *in vitro* cytotoxicity evaluation and hemolysis assay showed that the nanoparticles possessed good biocompatibility. Hardness investigations and AFM measurements indicated that both the sintering temperature and compression force played an important role in determining the physical behaviors (hardness, roughness and density) of flakes of the ZrO₂ nanoparticles. When ZrO₂ nanoparticles synthesized at 500 °C were pressed into flakes under 6 MPa and sintered at 1400 °C, the resulting flakes exhibited an optimal combination of hardness (534.58 gf·mm⁻²), roughness (0.07 μm) and density (4.41 g·cm⁻³). As the Vickers hardness value of human bones is of 315~535 gf·mm⁻² and the density of adult femur about 1.3~1.7 g·cm⁻³, the experimental results showed that the ZrO₂ flakes were comparable to human bones with a higher density. As a result, the synthesized ZrO₂ NPs may be useful for biomedical applications, especially for bone repair and replacement in future.

The field of biomaterial technology has rapidly progressed over the last few decades with the advent of advanced medical devices and implants developed from metals and ceramic¹. It is known that implantation of biomaterials also causes a cascade of reactions in the biological environment. For instance, the insertion of some implants may lead to bacterial infections along the bone/material interface due to poor biocompatibility of the implants despite total disinfection prior to the surgeries. After the bacterial proliferation period, the biomaterial-associated infections can hardly be cured by traditional systemic antibiotic therapy^{1,2}. Hence, there is a pressing need for the development of safe biocompatible implants. The success of rapid osseointegration of orthopedic implanted materials is dependent on the formation capability between the implants and bones, when the implants are embedded in living body³. Metal alloys (e.g., Ti, Sr, Co, Cr, etc.) are generally expected to be bioinert with biological systems in the human body. Consequently, implants made of metal alloys used in bone reconstruction typically lack desired osseointegration properties, which limits their biological fixation with bone tissues and consequently long-term *in vivo* stability⁴. Moreover, metal ions can be released from alloy implants due to its frequent interactions with the surrounding physiological environment, which may lead to detrimental effects on the long-term health of the patients¹⁻³.

Zirconia (ZrO₂), as one of the most important oxide materials, exhibits excellent properties including low thermal conductivity, high thermal expansion, good thermal stability, fine mechanical strength, good fracture toughness and high thermal shock resistance⁵⁻⁷. Thus, ZrO₂ has been used in a broad range of applications as catalysts/catalyst support⁸⁻¹⁴, oxygensensors^{11,12}, fuelcells^{13,14}, biological materials^{15,16}, automobile parts and thermal barrier coatings on metal components¹⁷⁻¹⁹. ZrO₂ nanomaterials have also been employed in medical and orthopedic applications, mainly for repair and replacement of diseased and damaged parts of human skeleton,

¹Laboratory for Micro-sized Functional Materials & College of Elementary Education, Capital Normal University, Beijing, 100048, PR China. ²Department of Chemistry, Capital Normal University, Beijing, 100048, PR China. ³Key Laboratory for Biomedical Effects of Nanomaterials and Nanosafety Institute of High Energy Physics, Chinese Academy of Sciences, Beijing, 100049, China. ⁴Department of Chemistry and Biochemistry, University of California, Santa Cruz, CA 95064, USA. *These authors contributed equally to this work. Correspondence and requests for materials should be addressed to Q.W. (email: qwchem@gmail.com) and S.C. (email: shaowei@ucsc.edu)

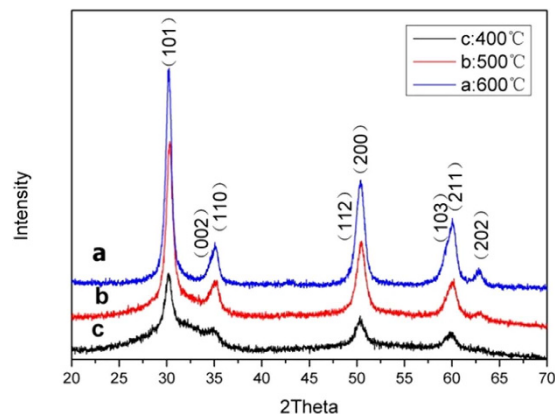


Figure 1. XRD patterns of ZrO₂ NPs synthesized at different temperatures.

bones, teeth and joints due to their good biocompatibility, osseointegration, and bioinertness²⁰. In fact, because of nontoxicity to the surrounding tissues, implants based on ZrO₂ nanoparticles (NPs) have been utilized for clinical total hip replacements, and as a prevalent biomaterial in prosthetic dentistry and dental implantology^{5,13,16,21,22}. This is largely ascribed to the good physical performance of sintered ZrO₂ devices, in terms of hardness, density, roughness and stability.

Currently, the synthetic methods of nano-sized ZrO₂ mainly include gas-phase methods (e.g., gas-phase chemical synthesis^{23–26} and chemical vapor deposition^{27–29}), and liquid-phase methods (fast precipitation^{30–33}, sol–gel^{34–36}, solvent evaporation, and hydrothermal treatment). However, up to now, reports remain scarce involving a comprehensive and detailed investigation of the sintering properties of ZrO₂ NPs under different conditions.

In this paper, ZrO₂ NPs were synthesized by using a simple vapor-phase hydrolysis process at controlled temperatures, and utilized to prepare nanoflakes by compression and sintering. By a systematic variation of the compression force and sintering temperature, the hardness and density of the resulting ZrO₂ nanoflakes were maximized whereas the roughness was minimized. The physical properties such as hardness, roughness as well as density of the sintered ZrO₂ nanoflakes were better than those of the human bone. Furthermore, *in vitro* cytotoxicity and hemolysis evaluation showed that the ZrO₂ NPs possessed good biocompatibility. These findings suggest great potential of the ZrO₂ NPs as a biompatible material for medical implants for bone tissue engineering because they meet the demand of high physical properties of artificial hard tissues.

Results

Structures of ZrO₂ NPs. The structures of the obtained ZrO₂ NPs were first characterized by X-ray diffraction (XRD) measurements. Figure 1 shows the XRD patterns of ZrO₂ NPs synthesized at different temperatures (400, 500 and 600 °C). A series of well-defined peaks can be identified at $2\theta = 30.2$, 35.0 , 50.4 , 60.0 and 62.7° , which were ascribed to the diffractions of the (101), (110), (200), (211), and (202) crystalline planes of cubic phase ZrO₂ (JCPDS card no. 49-1642)²¹, respectively. In addition, the asymmetric line shape of the peaks at 35.0 , 50.4 and 60.0° suggested the formation of a tetragonal phase. The shoulder at $2\theta = 34.5^\circ$ was the diffraction of the (002) crystalline plane of tetragonal phase ZrO₂ (JCPDS card no. 42-1164), and those at $2\theta = 50.2^\circ$ and 59.1° corresponding to the diffractions of the (112) and (103) crystalline planes¹⁹. Furthermore, from Fig. 1, it can be seen that the crystallinity of the ZrO₂ NPs increased with increasing synthesis temperature from 400 °C to 600 °C.

SEM Analysis. Further structural insights were obtained in SEM measurements. From Supporting Figure S1, it can be seen that the ZrO₂ NPs are mostly in the range of 15 to 65 nm in diameter. Statistical analysis based on more than 50 particles showed that the average diameter of the nanoparticles decreased with increasing synthesis temperature, 40 nm at 400 °C, 35 nm at 500 °C, and 30 nm at 600 °C, as manifested in the core size histograms (Supporting Figure S2).

In Vitro Cytotoxicity. Interestingly, the resulting ZrO₂ NPs were found to exhibit low cytotoxicity, as manifested in *in vitro* studies with human umbilical vein endothelial cells lines (HUVEC). Experimentally, ZrO₂ NPs were dispersed under sonication at varied concentration (up to $1 \text{ mg}\cdot\text{mL}^{-1}$) into dulbecco's modified eagle medium (DMEM) and added to the HUVEC cell culture. The *in vitro* cytotoxicity of the ZrO₂ NPs in HUVEC cells was evaluated by CCK-8 assay. Control experiments were also carried out by dispersing the ZrO₂ NPs in deionized water, and phosphate buffer saline (PBS) (Fig. 2). From Fig. 3, it can be seen that the ZrO₂ NPs (up to $500 \mu\text{g}\cdot\text{mL}^{-1}$) exerted virtually no effect on cell viability after co-incubation for 24 h. For example, the HUVEC cells retained 92% of viability even at the concentration of $500 \mu\text{g}\cdot\text{mL}^{-1}$ of ZrO₂ NPs synthesized at 400, 500, or 600 °C.

Hemolysis of the ZrO₂ NPs was also evaluated by incubating the NPs with red blood cells (RBCs) for 4 h. It can be seen that the hemolytic percentages of RBCs were lower than 3.6% for the NPs synthesized at 400, 500, and 600 °C even at the concentration as high as $800 \mu\text{g}\cdot\text{mL}^{-1}$, implying that these NPs had a negligible hemolytic activity (Fig. 4a–c). Therefore, it can be concluded that the ZrO₂ NPs exhibit good biocompatibility and thus can act as a promising bio-ceramic materials for prosthetic dentistry and dental implantology^{37,38}.

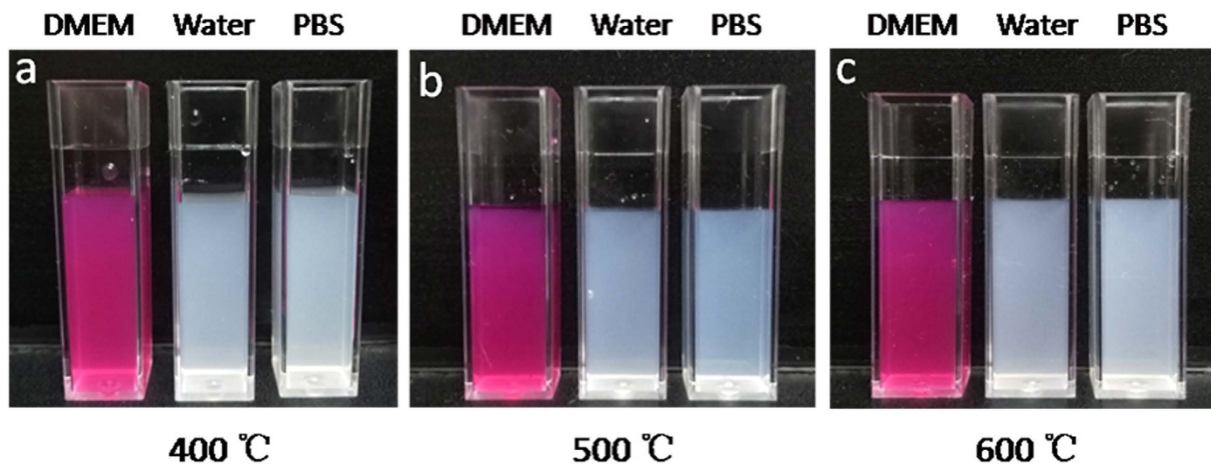


Figure 2. Photographs of ZrO_2 NPs dispersions in DMEM, Water, PBS. ZrO_2 NPs were synthesized at different temperatures (a) 400 °C, (b) 500 °C, and (c) 600 °C.

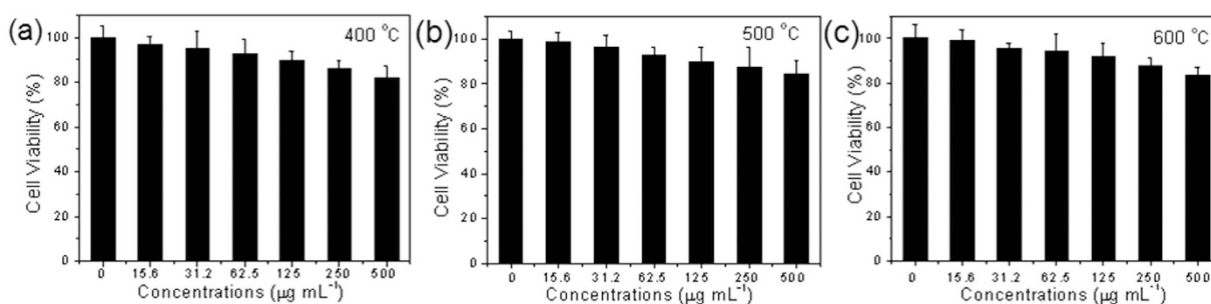


Figure 3. Cell viabilities of HUVEC cells after treatment with ZrO_2 NPs at various concentrations for 24 h.

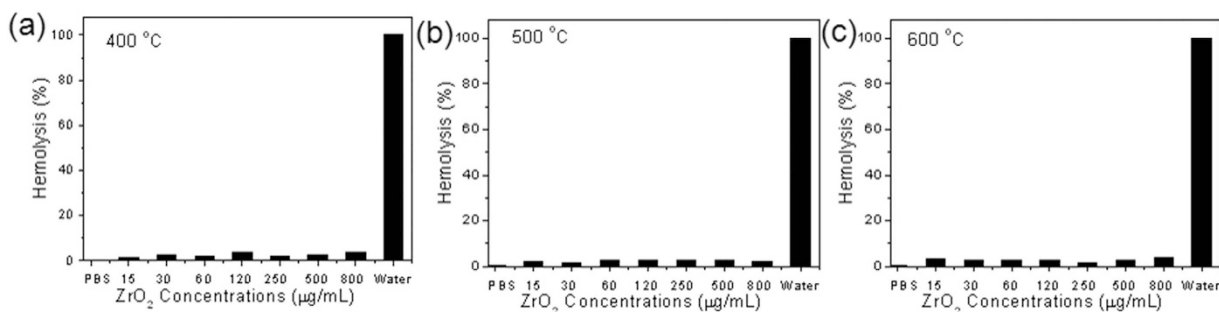


Figure 4. Hemolytic percent of RBCs. The RBCs was incubated with ZrO_2 NPs at various concentrations for 4 h, using deionized water and PBS as positive and negative controls, respectively.

Physical Hardness. With such remarkable cytocompatibility and hemocompatibility, ZrO_2 NPs-based materials may be viable candidates for biomedical applications. Thus, the ZrO_2 NPs were pressed into nanoflakes and subjected to sintering at elevated temperatures. Significantly, the obtained nanoflakes exhibited remarkable Physical characteristics. First, Vickers hardness tests were performed to examine the materials hardness, which was quantified by the peak load (P_{\max}) and projected contact area (A), $H = \frac{P_{\max}}{A}$.

The results were listed in Table 1. It can be seen that for ZrO_2 NPs prepared at 400 °C, at the same sintering temperature, there is a maximum hardness that varies with the compression force (Supporting Figure S3); and at the same compression force, there is also a maximum hardness that varies with the sintering temperature. The maximum hardness (603.25 gf·mm⁻²) could be found at the compression force of 3 MPa and sintering temperature of 1200 °C. Similarly, for the ZrO_2 NPs prepared at 500 and 600 °C, the maximum hardness can be identified at 3 MPa and 1200 °C, and 3 MPa and 1400 °C, respectively.

As is known, when the ZrO_2 NPs are pressed into flakes, at low compression forces the flakes are likely crack-free such that the hardness increases with increasing compression force; however, at too high a compression force, (micro) cracks would start to form in the flakes, leading to reduced hardness. Likewise, at relatively

C. Force							
Hardness							
Syn. Temp	S. Temp	2 MPa	3 MPa	6 MPa	10 MPa	14 MPa	18 MPa
400 °C	800 °C	150.28	411.64	200.55	286.30	332.89	324.56
	1000 °C	188.00	460.30	311.34	299.65	431.36	420.47
	1200 °C	543.85	603.25	440.13	467.03	460.85	454.70
	1400 °C	450.51	477.59	462.29	452.65	419.63	405.69
500 °C	800 °C	99.71	284.30	233.39	248.84	266.57	262.87
	1000 °C	103.38	331.60	387.94	375.85	357.65	356.67
	1200 °C	548.40	562.00	476.36	473.04	468.07	458.26
	1400 °C	383.63	542.62	534.58	477.21	468.65	460.44
600 °C	800 °C	195.33	343.27	133.21	263.46	251.32	246.58
	1000 °C	104.90	252.67	232.78	371.88	446.96	425.60
	1200 °C	575.50	621.30	492.09	502.75	530.99	408.04
	1400 °C	503.22	765.98	488.67	463.27	417.01	412.79

Table 1. Physical hardness ($\text{gf}\cdot\text{mm}^{-2}$) of ZrO_2 flakes. The ZrO_2 flakes prepared by compression of ZrO_2 NPs synthesized at 400, 500 and 600 °C under 2, 3, 6, 10, 14 and 18 MPa and sintering at 800, 1000, 1200 and 1400 °C (C. Force: compression forces, S. Temp: sintering temperature, Syn. Temp: Synthesis temperature).

low sintering temperatures, thermal stress in the particle cores was minimal and the flake hardness increased with increasing sintering temperature; in contrast, thermal stress became increasingly significant during high-temperature calcinations which led to the formation of cracks and hence reduced hardness^{39,40}. Taken together, these results suggest that both the compression force and sintering temperature play an important role in the determination of the hardness of the flakes, and the maximum hardness may be manipulated by sintering temperature and compression force.

Surface Roughness. The surface morphologies of the ZrO_2 nanoflakes were then analyzed by AFM measurements. From the AFM topographs in Fig. 5, the root mean square (rms) roughness of the ZrO_2 nanoflakes was evaluated as a function of sintering temperature and compression force⁴¹. Experimentally, the rms roughness was quantified by taking an average of five data points measured over an area of $4\mu\text{m} \times 4\mu\text{m}$ (Table 2). It can be seen that under the same compression force, the surface roughness of the flakes diminished with increasing sintering temperature (Supporting Figure S4).

From Table 2, it can also be seen that at the same sintering temperature, the roughness of the flakes remained almost invariant with the compression force. Yet, at a constant compression force, the roughness of the flakes decreased with increasing sintering temperature, consistent with the results in Fig. 5. Interestingly, at the same sintering temperature, the ZrO_2 surface roughness remained almost constant (Fig. 6), independent of the compression force. With increasing sintering temperature, the ZrO_2 NPs tended to agglomerate and the surface roughness decreased accordingly. It has been reported that the surface properties play a critical role in the stability and function of bone-rebuilding materials³⁹. Thus, changing the sintering temperature to reduce flakes roughness may enhance the biomedical applications of the ZrO_2 flakes.

Flake Density. Density is another important parameter in the assessment of materials for biomedical implants. The density of the ZrO_2 nanoflakes was quantitatively evaluated by using a precision electronic hydrometer^{42,43}, and the results are summarized in Table 3.

One can see that the density of the flakes varied with the sintering temperature and compression force, ranging from 2 to $7\text{ g}\cdot\text{cm}^{-3}$, much higher than that of adult femurs ($1.3\sim 1.7\text{ g}\cdot\text{cm}^{-3}$)^{44,45}.

From the above studies, one can see that when ZrO_2 NPs synthesized at 500 °C were pressed into flakes under the compression force of 6 MPa and sintered at 1400 °C, the resulting flakes exhibited an optimal combination of hardness ($534.58\text{ gf}\cdot\text{mm}^{-2}$), roughness ($0.07\mu\text{m}$) and density ($4.41\text{ g}\cdot\text{cm}^{-3}$), considering that the highest hardness value for human bones is between 4 to $5\text{ gf}\cdot\text{mm}^{-2}$, corresponding to Vickers hardness between 315 to $535\text{ gf}\cdot\text{mm}^{-2}$, whereas the density of adult femurs of $1.3\sim 1.7\text{ g}\cdot\text{cm}^{-3}$ ⁴⁴⁻⁴⁶. At this optimal point, the flakes hardness is comparable to that of the human skeleton while the density is far larger. Thus, the ZrO_2 flakes may be used as biological materials for hip replacements, rosthetic dentistry and dental implantology. This is being pursued in ongoing studies.

Discussion

ZrO_2 NPs were synthesized by a simple vapor-phase hydrolysis process⁴⁷. Vickers hardness investigation indicated that both the sintering temperature and compression force played an important role in the determination of the hardness of the ZrO_2 flakes. AFM studies showed that the surface roughness of the ZrO_2 flakes gradually decreased with increasing sintering temperature. In addition, the density of the ZrO_2 flakes was also determined within the context of sintering temperature and compression force. With a systematic variation of these two parameters, hardness and density of the ZrO_2 nanoflakes were maximized and roughness was minimized simultaneously^{48,49}. When ZrO_2 NPs synthesized at 500 °C were pressed into flakes under the compression force of 6 MPa

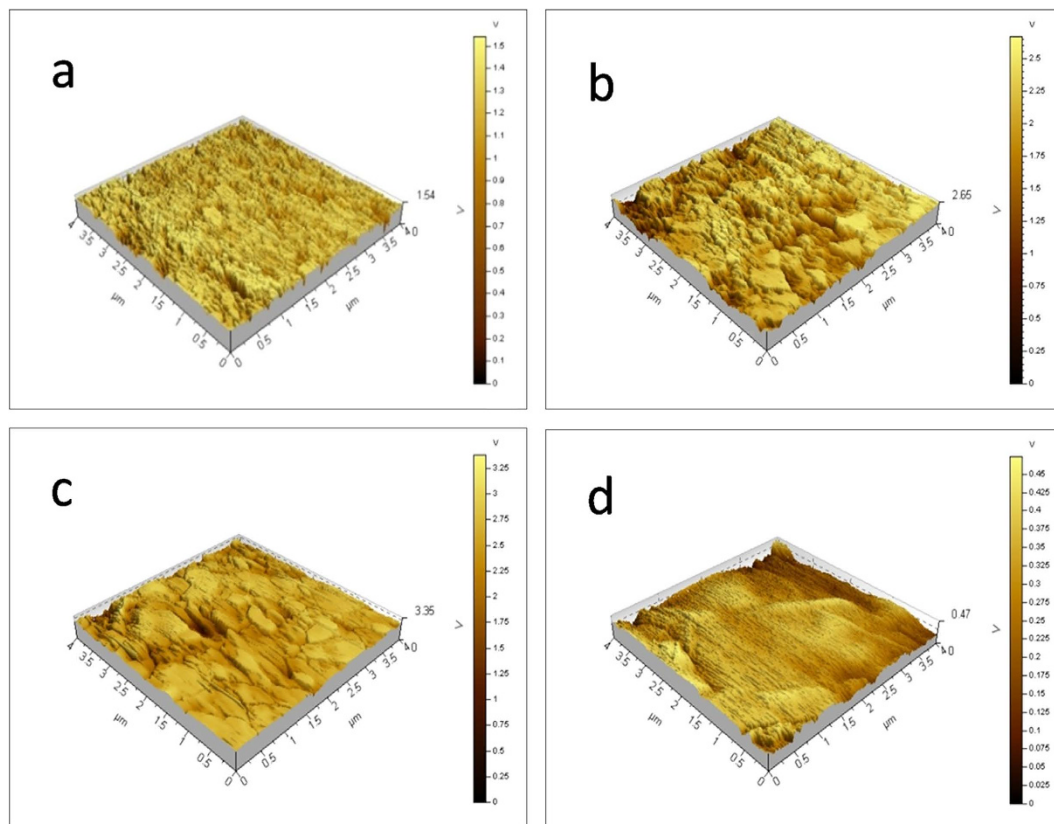


Figure 5. AFM images of ZrO_2 flakes. The ZrO_2 flakes were prepared by compression at 18 MPa of ZrO_2 NPs synthesized at 400 °C and sintering at various temperatures: (a) 800 °C, (b) 1000 °C, (c) 1200 °C and (d) 1400 °C.

C. Force							
Rms. Roughness							
Syn. Temp	S. Temp	2 MPa	3 MPa	6 MPa	10 MPa	14 MPa	18 MPa
400 °C	800 °C	0.22	0.40	0.45	0.29	0.21	0.22
	1000 °C	0.18	0.32	0.23	0.23	0.16	0.21
	1200 °C	0.17	0.29	0.27	0.22	0.22	0.19
	1400 °C	0.14	0.13	0.21	0.10	0.07	0.12
500 °C	800 °C	0.30	0.47	0.37	0.56	0.65	0.22
	1000 °C	0.19	0.25	0.30	0.33	0.26	0.21
	1200 °C	0.18	0.33	0.26	0.34	0.24	0.15
	1400 °C	0.05	0.16	0.07	0.07	0.07	0.08
600 °C	800 °C	0.15	0.51	0.28	0.47	0.29	0.20
	1000 °C	0.25	0.13	0.25	0.26	0.23	0.19
	1200 °C	0.22	0.24	0.38	0.27	0.21	0.11
	1400 °C	0.07	0.09	0.08	0.13	0.13	0.06

Table 2. Surface roughness (μm) of ZrO_2 flakes. The ZrO_2 flakes prepared by compression of ZrO_2 NPs synthesized at 400, 500 and 600 °C under 2, 3, 6, 10, 14 and 18 MPa and sintering at 800, 1000, 1200 and 1400 °C.

and sintering at 1400 °C, the resulting flakes exhibited an optimal combination of hardness ($534.58 \text{ gf}\cdot\text{mm}^{-2}$), roughness ($0.07 \mu\text{m}$) and density ($4.41 \text{ g}\cdot\text{cm}^{-3}$).

In conclusion, the experimental results show that both the sintering temperature and compression force played an important role in determining the physical behaviors (hardness, roughness, and density) of ZrO_2 flakes. Thus, by changing compression force and sintering temperature, the hardness parameters of the ZrO_2 flakes can be adjusted and comparable to those of human bones, along with a higher density. More importantly, the *in vitro* cytotoxicity and hemolysis evaluation shows that the ZrO_2 NPs have good biocompatibility. Therefore, it is believed the ZrO_2 NPs have promising application for bone tissue engineering and regenerative medicine.

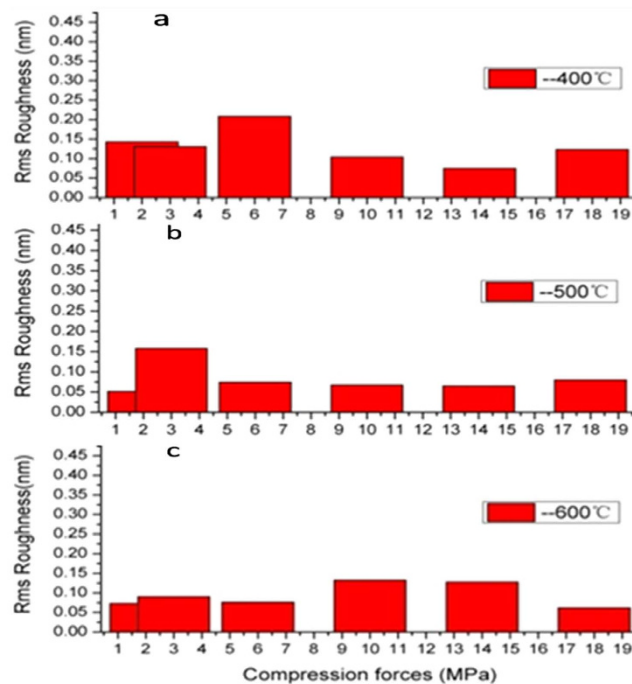


Figure 6. Surface roughness of ZrO₂ flakes. The ZrO₂ flakes prepared by sintering at 1400 °C under different compression forces of ZrO₂ NPs synthesized at different temperatures (a) 400 °C, (b) 500 °C, and (c) 600 °C.

C. Force							
Density							
S. Temp	Syn. Temp	2 MPa	3 MPa	6 MPa	10 MPa	14 MPa	18 MPa
800 °C	400 °C	3.47	3.80	4.57	3.68	3.78	4.95
	500 °C	4.38	3.09	3.20	4.11	5.69	5.86
	600 °C	3.50	3.85	2.59	3.87	6.05	5.60
1000 °C	400 °C	3.58	3.56	4.55	4.45	5.58	5.28
	500 °C	4.04	4.63	4.24	5.66	5.55	6.33
	600 °C	3.76	3.57	5.44	5.94	5.29	6.38
1200 °C	400 °C	5.53	4.43	4.42	3.64	5.52	4.56
	500 °C	4.85	5.43	7.40	4.87	6.15	5.28
	600 °C	3.64	3.40	3.86	5.40	4.68	2.58
1400 °C	400 °C	3.94	3.90	3.18	5.36	5.62	5.28
	500 °C	2.91	3.79	4.41	4.60	5.15	4.87
	600 °C	3.09	2.24	5.23	4.77	3.67	5.12

Table 3. Density (g·cm⁻³) of ZrO₂ flakes. The ZrO₂ flakes prepared by compression of ZrO₂ NPs synthesized at 400, 500 and 600 °C under 2, 3, 6, 10, 14 and 18 MPa and sintering at 800, 1000, 1200 and 1400 °C.

Methods

Material Preparation. ZrO₂ NPs were synthesized by a vapor-phase hydrolysis procedure and the experimental apparatus had been reported in a previous study⁴⁷. In brief, the reactor was made of two glass tubes that were externally heated in a vertical furnace. ZrCl₄ was sublimated at 350 °C and carried by a N₂ gas (99.9%) into the reaction chamber via the nozzle. Water vapor was introduced into the reaction chamber from around the nozzle by dry air. These two gas streams were mixed rapidly, reacted, and formed ZrO₂ NPs at atmospheric pressure. Then, the aerosol was cooled by a water jacket tube and filtered at the exit of the reactor for analysis, followed by washing. Three samples of ZrO₂ NPs were synthesized at different temperatures (400, 500 and 600 °C) and pressed into flakes at different compression force (2, 3, 6, 10, 14 and 18 MPa), which were then subjected to sintering for 6 h at 800, 1000, 1200 and 1400 °C, respectively.

Cell Culture and Cytotoxicity Evaluation. Human umbilical vein endothelial cells lines (HUVEC) were used to evaluate the cytotoxicity of ZrO₂ NPs. The cells were cultured in a complete medium Dulbecco's modified Eagle's medium (DMEM) containing 10% fetal bovineserum (FBS, GIBCO) and streptomycin/penicillin

(100 $\mu\text{g}\cdot\text{mL}^{-1}$ Hyclone) at 37 °C in amoisturized 5% CO₂ incubator. The viability of the treated cells was measured by the Cell Counting Kit-8 (CCK-8) assay. Firstly, HUVEC cells were seeded into a 96-well cell culture plates at the densities of 2×10^4 cells/well, in 100 μL of a complete culture medium at 37 °C for 24 h. Afterward, the ZrO₂ NPs dispersions were diluted with a fresh medium to the desired concentrations and then added to each well to replace the original culture medium. After another 24 h, the culture medium was removed and replaced by 10 μL of CCK-8 in serum-free media. After incubation for 2 h at 37 °C, the optical density of each well was read at 450 nm on a microplate reader (Spectra Max M2MDC, USA)^{37,50–54}.

Hemolysis Assay of ZrO₂ NPs were carried out as follows. Kunming mice (5 weeks old) were purchased from Vital River (Beijing, China) and the whole blood was obtained from the mice. All the animals experiments were performed in accordance with the guideline and regulation for the care and use of laboratory animals of Ministry of Science and Technology of People's Republic of China's requirements. The Animal Study Committee of the Ministry of Science and Technology of the People's Republic of China has approved the experiments. Briefly, mice blood were centrifuged and diluted 10 times with PBS to obtain red blood cells (RBCs). Then, 0.2 mL of diluted RBCs were added to 0.8 mL of PBS containing ZrO₂ NPs at various concentrations (15, 30, 60, 120, 250, 500, and 800 $\mu\text{g}\cdot\text{mL}^{-1}$), 0.8 mL of distilled water (positive control), and 0.8 ML of PBS (negative control), respectively. After that, the mixtures were kept at room temperature for 4 h, before they were centrifuged at 12000 rpm for 3 min. Absorbance of the supernatants was measured by a UV-vis spectrophotometer and hemolysis percentage of RBCs was calculated based on the absorbance at 541 nm using equation (1):

$$\text{Hemolysis(\%)} = \frac{A_{\text{sample}} - A_{0\%}}{A_{100\%} - A_{0\%}} \times 100\% \quad (1)$$

where A_{sample} , $A_{0\%}$ and $A_{100\%}$ are the absorbance of the supernatant of the samples, the negative control, and positive control, respectively.

Materials Characterizations. The composition, morphologies of the nanoparticles prepared above were characterized by X-ray powder diffraction (XRD, Bruker D8, Cu K α radiation, $\lambda = 1.54 \text{ \AA}$). The size distribution and morphology of the nanoparticles were examined by scanning electron microscopy (SEM, HITACHI, S4800, 15 kV) studies. The hardness of the flakes was evaluated by using a Vickers hardness instrument (UHL Microhardness Testers VMHT. VMH-001) equipped with a cube-corner diamond tip, where the sintered flakes were cleaned by a stream of high-purity nitrogen. To minimize substrate contributions, the indentation experiments were performed in load control, with the load of 50 gf. The loading and unloading speed was $5 \times 10^{-6} \text{ m}\cdot\text{s}^{-1}$, and the time under the peak load was 15 s^{48,49,55–58}. Ten random tests were performed for each sample to evaluate the material hardness. The surface morphology was analyzed using AFM and the rms roughness was obtained for the ZrO₂ flakes. The rms roughness data were obtained over an area of $4 \mu\text{m} \times 4 \mu\text{m}$ at five different points of the sample and averaged^{57,59,60}. The density of the flakes was characterized with a precision electronic hydrometer (DH-120M) by equation (2),

$$\rho = \frac{I.M.}{I.M. - M.M.} \times \rho_{\text{H}_2\text{O}} \quad (2)$$

where ρ is the density of the flakes, $I.M.$ is inherent mass, $M.M.$ is measured mass of the flasks and $\rho_{\text{H}_2\text{O}}$ is the density of water at 20 °C.

References

- Holzappel, B. M. *et al.* How smart do biomaterials need to be? A translational science and clinical point of view. *Adv. Drug Delivery Rev.* **65**, 581–603 (2013).
- He, G. P. *et al.* Addition of Zn to the ternary Mg–Ca–Sr alloys significantly improves their antibacterial properties. *J. Mater. Chem. B* **3**, 6676–6686 (2015).
- Xu, J., Liu, L. L., Munroe, P. & Xie, Z. H. Promoting bone-like apatite formation on titanium alloys through nanocrystalline tantalum nitride coatings. *J. Mater. Chem. B* **3**, 4082–4094 (2015).
- Roy, M., Balla, V. K., Bandyopadhyay, A. & Bose, S. MgO-Doped Tantalum Coating on Ti: Microstructural Study and Biocompatibility Evaluation. *Mater. Interfaces* **4**, 577–580 (2012).
- Kelly, J. R. & Denry, I. Stabilized zirconia as a structural ceramic: An overview. *Dent. Mater.* **24**, 289–298 (2008).
- Gu, X. Y., Li, X., Liu, Q., Chen, Y. X. & Li, Y. X. Effects of Calcium Acetate on the Hydrothermal Synthesis of Tetragonal-Phase ZrO₂ (3Y) Nanocrystals. *Rare Met. Mater. Eng.* **38**, 1044–1066 (2009).
- Liu, X. Y., Chu, P. K. & Ding, C. X. Surface nano-functionalization of biomaterials. *Mater. Sci. Eng. R* **70**, 275–302 (2010).
- Lee, H. S., Huy, C. N., Pham, T. T. & Shin, E. W. ZrO₂-impregnated red mud as a novel catalyst for steam catalytic cracking of vacuum residue. *Fuel* **165**, 462–467 (2016).
- Harju, H., Lehtonen, J. & Lefferts, L. Steam reforming of *n*-butanol over Rh/ZrO₂ catalyst: role of 1-butene and butyraldehyde. *Appl. Catal. B* **182**, 33–46 (2016).
- Goscianska, J., Ziolk, M., Gibson, E. & Daturi, M. Meso-macroporous zirconia modified with niobia as support for platinum—Acidic and basic properties. *Catal. Today* **152**, 33–41 (2010).
- Ward, D. A. & Ko, E. I. Preparing Catalytic Materials by the Sol-Gel Method. *Ind. Eng. Chem. Res.* **34**, 421–433 (1995).
- Li, Y. W. *et al.* Effect of calcium salts on isosynthesis over ZrO₂ catalysts. *J. Mol. Catal. A: Chem.* **175**, 267–275 (2001).
- Viazzi, C., Bonino, J. P. & Ansart, F. Synthesis by sol-gel route and characterization of Yttria Stabilized Zirconia coatings for thermal barrier applications. *Surf. Coat. Technol.* **201**, 3889–3893 (2006).
- Mazzoni, A. D. & Conconi, M. S. Study of carbonitriding reactions of zirconia. Synthesis of Zr (C, N, O) phases and β -type zirconium oxynitrides. *Ceram. Int.* **30**, 23–29 (2004).
- Ravichandran, K. S., An, K., Dutton, R. E. & Semiatin, S. L. Thermal conductivity of plasma-sprayed monolithic and multilayer coatings of alumina and yttria-stabilized zirconia. *J. Am. Ceram. Soc.* **82**, 673–682 (1999).
- Korotcenkov, G., Han, S. D. & Stetter, J. R. Review of Electrochemical Hydrogen Sensors. *Chem. Rev.* **109**, 1402–1433 (2009).
- Subbarao, E. C. & Maiti, H. S. Oxygen sensors and pumps. *Adv. Ceram.* **24**, 731–747 (1988).

18. Manicone, P. F., Iommetti, P. R. & Raffaelli, L. An overview of zirconia ceramics: Basic properties and clinical applications. *J. Dent.* **35**, 819–826 (2007).
19. Wang, Y. Q. & Sayre, G. Commercial thermal barrier coatings with a double-layer bond coat on turbine vanes and the process repeatability. *Surf. Coat. Technol.* **203**, 2186–2192 (2009).
20. Thamaraiselvi, T. V. & Rajeswari, S. Biological evaluation of bioceramic materials. *Trends Biomater. Artif. Organs* **18**, 9–17 (2004).
21. He, G. P. *et al.* Addition of Zn to the ternary Mg–Ca–Sr alloys significantly improves their antibacterial properties. *J. Mater. Chem. B* **3**, 6676–6689 (2015).
22. Xu, J., Liu, L. L., Munroe, P. & Xie, Z. H. Promoting bone-like apatite formation on titanium alloys through nanocrystalline tantalum nitride coatings. *J. Mater. Chem. B* **3**, 4082–4094 (2015).
23. Xia, B., Duan, L. Y. & Xie, Y. C. ZrO₂ nanopowders prepared by low-temperature vapor-phase hydrolysis. *J. Am. Ceram. Soc.* **83**, 1077–1080 (2000).
24. Fang, Z. T. & Dixon, D. A. Hydrolysis of ZrCl₄ and HfCl₄: The Initial Steps in the High-Temperature Oxidation of Metal Chlorides to Produce ZrO₂ and HfO₂. *J. Phys. Chem. C* **117**, 7459–7474 (2013).
25. Suyama, Y., Mizobe, T. & Kato, A. ZrO₂ Powders Produced by Vapor Phase Reaction. *Ceramurgia Int.* **3**, 141–146 (1977).
26. Mazdiyasi, K. S., Lynch, C. T. & Smith, J. S. Preparation of Ultra-High-Purity Submicron Refractory Oxides. *J. Am. Ceram. Soc.* **48**, 372–375 (1965).
27. Tok, A. I. Y., Boey, F. Y. C., Duand, S. W. & Wong, B. K. Flame spray synthesis of ZrO₂ nano-particles using liquid precursors. *Mater. Sci. Eng. B* **130**, 114–119 (2006).
28. Esparza-Ponce, H. E., Reyes-Rojas, A., Antúnez-Flores, W. & Miki-Yoshida, M. Synthesis and characterization of spherical calcia stabilized zirconia nano-powders obtained by spray pyrolysis. *Mater. Sci. Eng. A* **343**, 82–88 (2003).
29. Burleson, D. J., Roberts, J. T., Gladfelter, W. L., Campbell, S. A. & Smith, R. C. A Study of CVD Growth Kinetics and Film Microstructure of Zirconium Dioxide from Zirconium Tetra-*tert*-Butoxide. *Chem. Mater.* **14**, 1269–1276 (2002).
30. Chandra, N. *et al.* Synthesis and characterization of nano-sized zirconia powder synthesized by single emulsion-assisted direct precipitation. *J. Colloid Interface Sci.* **342**, 327–332 (2010).
31. Wang, S. Y., Li, X. A., Zhai, Y. C. & Wang, K. M. Preparation of homodispersed nano zirconia. *Powder Technol.* **168**, 53–58 (2006).
32. Rezaei, M., Alavi, S. M., Sahebdehfar, S. & Yan, Z. F. Tetragonal nanocrystalline zirconia powder with high surface area and mesoporous structure. *Powder Technol.* **168**, 59–63 (2006).
33. Hsu, Y. W., Yang, K. H., Chang, K. M., Yeh, S. W. & Wang, M. C. Synthesis and crystallization behavior of 3 mol% yttria stabilized tetragonal zirconia polycrystals (3Y-TZP) nanosized powders prepared using a simple co-precipitation process. *J. Alloys Compd.* **509**, 6864–6870 (2011).
34. Tahmasebpour, M., Babaluo, A. A. & Aghjeh, M. K. R. Synthesis of zirconia nanopowders from various zirconium salts via polyacrylamide gel method. *J. Eur. Ceram. Soc.* **28**, 773–778 (2008).
35. Heshmatpour, F. & Aghakhanpour, R. B. Synthesis and characterization of superfine pure tetragonal nanocrystalline sulfated zirconia powder by a non-alkoxide sol–gel route. *Adv. Powder Technol.* **23**, 80–87 (2012).
36. Dwivedi, R., Maurya, A., Verma, A., Prasada, R. & Bartwal, K. S. Microwave assisted sol–gel synthesis of tetragonal zirconia nanoparticles. *J. Alloys Compd.* **509**, 6848–6851 (2011).
37. Yin, W. Y., Yan, L., Yu, J. & Tian, G. High-Throughput Synthesis of Single-Layer MoS₂ Nanosheets as a Near-Infrared Photothermal-Triggered Drug Delivery for Effective Cancer Therapy. *ACS nano*, **8**, 6922–6933 (2014).
38. Song, M. M., Song, W. J., Bi, H. & Wang, J. Cytotoxicity and cellular uptake of iron nanowires. *Biomaterials* **31**, 1509–1517 (2010).
39. Cho, S. M. *et al.* Multifunctional Composite Coating as a Wear-Resistant Layer for the Bearing in Total Hip Joint Replacement. *ACS Appl. Mater. Interfaces* **5**, 395–403 (2013).
40. Clausell, C., Barba, A., Nuno, L. & Jarque, J. C. Effect of average grain size and sintered relative density on the imaginary part – μ'' of the complex magnetic permeability of (Cu_{0.12}Ni_{0.23}Zn_{0.65}) Fe₂O₄ system. *Ceramics International* **42**, 4256–4261 (2016).
41. Arias, D. F., Arango, Y. C. & Devia, A. Study of TiN and ZrN thin films grown by cathodic arc technique. *Applied Surface Science* **253**, 1683–1690 (2006).
42. Liu, B., Xiao, H. Y., Zhang, Y. W., Aidhy, D. S. & Weber, W. J. Investigation of oxygen point defects in cubic ZrO₂ by density functional theory. *Computational Materials Science* **92**, 22–27 (2014).
43. Negara, M. A., Goel, N., Bauza, D., Ghibauda, G. & Hurley, P. K. Interface state densities, low frequency noise and electron mobility in surface channel In_{0.53}Ga_{0.47}As *n*-MOSFETs with a ZrO₂ gate dielectric. *Microelectronic Engineering* **88**, 1095–1097 (2011).
44. Wen, J. G., Liu, Y., Liao, X., Shi, L. J. & Liu, J. Y. An investigation of bone density among children aged over 5 years old in Shenyang city. *Chinese Journal of Woman and Child Health Research* **19**, 15–16 (2008).
45. Zhang, J. H., Wang, L. & Wang, Y. L. Investigation of bone mineral density in punching and welding workers. *Chin J Osteoporos* **21**, 706–707 (2015).
46. Zhang, M. M., Li, Y. G. & Liu, Y. Study on the influencing factors for bonemineral density among 24831 people in Changchun. *Chin J Osteoporos* **16**, 125–127 (2010).
47. Wang, Q. & Li, C. H. Controllable synthesis of zirconia nano-powders using vapor-phase hydrolysis and theoretical analysis. *J. Mater. Chem. A* **2**, 1346–1352 (2014).
48. Julietta, V. R. *et al.* Physicochemical Investigation of Pulsed Laser Deposited Carbonated Hydroxyapatite Films on Titanium. *ACS Appl. Mater. Interfaces* **1**, 1813–1820 (2009).
49. Oliver, W. C. & Pharr, G. M. An improved technique for determining hardness and elastic modulus using load and displacement sensing indentation experiments. *J. Mater. Res.* **7**, 1564–1583 (1992).
50. Zhang, F. *et al.* A Novel High Mechanical Property PLGA Composite Matrix Loaded with Nanodiamond–Phospholipid Compound for Bone Tissue Engineering. *ACS Appl. Mater. Interfaces* **8**, 1087–1097 (2016).
51. Chandra, V. S., Baskar, G., Suganthi, R. V. & Elayaraja, K. Blood Compatibility of Iron-Doped Nanosize Hydroxyapatite and Its Drug Release. *ACS Appl. Mater. Interfaces* **4**, 1200–1210 (2012).
52. Zhang, Z. Q. *et al.* The influence of UV irradiation on the biological properties of MAO-formed ZrO₂. *Colloids. Surf. B* **89**, 40–47 (2012).
53. Catauro, M. *et al.* Biological response of human mesenchymal stromal cells to titanium grade 4 implants coated with PCL/ZrO₂ hybrid materials synthesized by sol–gel route: *in vitro* evaluation. *Mater. Sci. Eng. C* **45**, 395–401 (2014).
54. Wang, Y., Yu, H. J., Chen, C. Z. & Zhao, Z. H. Review of the biocompatibility of micro-arc oxidation coated titanium alloys. *Materials and Design*, **85**, 640–652 (2015).
55. Garvie, R. C. & Nicholson, P. S. Phase Analysis in Zirconia Systems. *J. Am. Ceram. Soc.* **55**, 303–305 (1972).
56. Cabibbo, M. *et al.* An international round-robin calibration protocol for nanoindentation measurements. *Micron*, **43**, 215–222 (2012).
57. Dorcioman, G., Socol, G., Craciun, D. & Argibay, N. Wear tests of ZrC and ZrN thin films grown by pulsed laser deposition. *Appl. Surf. Sci.* **306**, 33–36 (2014).
58. Craciun, D. *et al.* Thin and hard ZrC/TiN multilayers grown by pulsed laser deposition. *Surf. Coat. Technol.* **205**, 5493–5496 (2011).
59. Craciun, D. *et al.* Characteristics of ZrC/ZrN and ZrC/TiN multilayers grown by pulsed laser deposition. *Appl. Surf. Sci.* **257**, 5332–5336 (2011).
60. Thornton, A. J. High rate thick film growth. *Ann. Rev. Mater. Sci.* **7**, 239–260 (1977).

Acknowledgements

This work was supported by the Natural Science Foundation of China (No. 21471103, 51002180, and 11275218), National Basic Research Programs of China (973 program, No. 2015CB932104), the Project of Excellent Talents of Beijing (No. 203135407707), Beijing Natural Science Foundation (No. 2162046), and the Scientific Research Base Development Program of the Beijing Municipal Commission of Education.

Author Contributions

J.W. and W.Y. conducted the experiment, J.W. and W.Y. wrote the manuscript. Q.W., S.C., X.H. and M.G. discussed and reviewed the manuscript.

Additional Information

Supplementary information accompanies this paper at <http://www.nature.com/srep>

Competing financial interests: The authors declare no competing financial interests.

How to cite this article: Wang, J. *et al.* Good Biocompatibility and Sintering Properties of Zirconia Nanoparticles Synthesized via Vapor-phase Hydrolysis. *Sci. Rep.* **6**, 35020; doi: 10.1038/srep35020 (2016).



This work is licensed under a Creative Commons Attribution 4.0 International License. The images or other third party material in this article are included in the article's Creative Commons license, unless indicated otherwise in the credit line; if the material is not included under the Creative Commons license, users will need to obtain permission from the license holder to reproduce the material. To view a copy of this license, visit <http://creativecommons.org/licenses/by/4.0/>

© The Author(s) 2016